C. R. Mecanique 342 (2014) 208–219

Contents lists available at ScienceDirect

Comptes Rendus Mecanique

www.sciencedirect.com

Micromechanics of granular materials – A tribute to Ching S. Chang

Numerical prediction of soil compaction in geotechnical engineering

Kaiming Xia

Shell Exploration & Production Company, 3333 Highway 6 S, Houston, TX 77001-0481, USA

ARTICLE INFO

Article history:
Available online 24 February 2014

Keywords:
Soil compaction
Large deformation
Finite element
Spatial density

ABSTRACT

Soil compaction involves a reduction in volume of the soil mass instead of settlement, which has been considered as one of the most important methods to increase geomaterials' strength in geotechnical engineering practice. This paper presents a numerical model to simulate soil compaction using the finite-element method with finite deformation. The fundamental formulations for soil compaction are introduced first. Then the model is employed to simulate the compaction process and predict spatial density, in which the soil is modeled as elastoplastic material. The Drucker–Prager/Cap model is integrated in the large-deformation finite-element code and used to model the gradual compaction process of soil. Representative simulations of practical applications in geotechnical/pavement engineering are provided to demonstrate the feasibility of predicting soil compaction density using the proposed large-deformation finite-element model.

1. Introduction

Soil compaction is a mechanical process by which mass of soil consisting of solid soil particles, air, and water is reduced in volume by the momentary application of loads, such as rolling, and vibration. Compaction of soils generally increases their shear strength, and decreases their compressibility and permeability. Soil compaction should be differentiated between cohesive soil (e.g., clay) and cohesionless soil (granular materials), which will be compacted using different compaction methods. Cohesive soils contain sufficient quantities of silt or clay to render soil mass virtually impermeable when properly compacted. Clay can be compacted using sheep foot compactor. Cohesionless soils include sand and gravel with relatively larger particle diameter can be compacted using vibratory compactor, and they still remain pervious even after being well compacted. An important characteristic of cohesive soils is that compaction improves their shear strength and compressibility properties. In geotechnical engineering, laboratory compaction standards have been followed to compact cohesive soils, such as Standard Proctor, which is used to estimate the maximum density of soils. For each compaction procedure, there exists an optimum water content, which corresponds to the maximum dry density. At any other water content, the resultant dry density is less than the maximum density.

During the past few decades, soil compaction has received increasing attention in the field of terramechanics, geotechnical and pavement engineering. The majority of research efforts has been focused on experimental device developments and field testing [1,2]. Some analytical and empirical approaches on soil compaction were also investigated [3–7]. These developments have facilitated the development of soil compaction technology and are beneficial to pavement construction.

E-mail address: kaiming.xia@gmail.com.

http://dx.doi.org/10.1016/j.crme.2014.01.007
1631-0721/

However, these analytical models oversimplify the dynamic soil/roller interaction, and therefore do not accurately capture the dynamic compaction process. It becomes evident that more efforts are needed for developing numerical models for soil compaction. As a robust numerical tool, the finite-element method has widely been used for stress and deformation analysis. The finite-element method has also been effectively applied to predict soil compaction [8–10].

Based on the available literature on geomaterial compaction, it seems that although the finite element has been used to study soil/asphalt compaction the background theory was not well introduced. It is therefore necessary more efforts should be devoted to developing efficient numerical model for soil compaction. This paper focuses on introducing the fundamental finite-element formulations for drained soil compaction. This paper is organized as follows. First, the fundamental formulation of large deformation for the calculation of density is introduced, which is followed by the introduction of the linearized weak form for updated Lagrangian formulation and finite-element formulation. The numerical integration of the constitutive equation for large deformation is then presented. Several numerical example studies are provided to demonstrate the efficiency of the numerical approach. Concluding remarks are finally presented based on the findings from this study.

2. Finite deformation and change of density

In order to predict the density change, it is necessary to recognize that the deformation of the soil medium could be relatively large during a loading–unloading cycle. This necessitates the clear distinction between the undeformed configuration and deformed configuration after soil compaction. For a typical time step, the updated configuration of the body at step $t_n + \Delta t$ may be written as a function of the configuration at step t_n and the incremental displacement $\Delta\mathbf{u}$ during the time step Δt. When common origins and directions for the coordinate configurations are used, an updated position vector can be given as

$$\mathbf{x}_{n+1} = \mathbf{X} + \mathbf{u} = \mathbf{x}_n + \Delta\mathbf{u} \tag{1}$$

where $\mathbf{u}$ is the total displacement vector with respect to the original configuration. The deformation gradient or intermediate deformation gradient is defined as follows:

$$\mathbf{F} = \frac{\partial\varphi}{\partial\mathbf{X}} = \mathbf{1} + \frac{\partial\mathbf{u}}{\partial\mathbf{X}} \quad \text{or} \quad f = \frac{\partial x_{n+1}}{\partial x_n} \tag{2}$$

where $\mathbf{1}$ is the identity unit tensor. Ω_{n+1} denotes the current configuration for updated Lagrangian formulation and the reference configuration is denoted by Ω_0. The volume relationship between reference and current configurations can be established as

$$\mathrm{d}\Omega_{n+1} = \det\mathbf{F}_{n+1}\,\mathrm{d}\Omega_0 = J_{n+1}\,\mathrm{d}\Omega_0 \tag{3}$$

Therefore, with the large-deformation updated Lagrangian formulation, one can predict the density change or compaction. In updated Lagrangian formulation, an incremental displacement is defined with respect to the configuration at time t_n, which is considered as the reference configuration for the current load step. The updated Lagrangian formulation can therefore be visualized as a series of intermediate total Lagrangian formulations. Based on the mass conservation, the relative compaction density can be updated at time t_{n+1} by

$$\rho_{n+1} = \frac{\rho_0}{\mathrm{Det}F_{n+1}} \quad \text{or} \quad \rho_{n+1} = \frac{\rho_n}{\mathrm{Det}f_{n+1}} \tag{4}$$

Here ρ_0 is the initial density and ρ_{n+1} is the relative density at time step t_{n+1}. Therefore, large-deformation analysis has many advantages in predicting soil compaction in civil engineering.

3. Updated Lagrangian formulation

Continuum based formulations for large deformation analysis can be written either in the material or in the spatial configuration. Discretization of the formulations written in the material/referential configuration or in the spatial/current configuration leads to the so-called total-Lagrangian or the updated-Lagrangian method, respectively. The principle of virtual work consisting of internal and external work can be expressed in the reference configuration at time t_0 as:

$$\delta W(\delta\mathbf{u}, V_0) = \int_{V_0} \mathbf{S} : \delta\mathbf{E}\,\mathrm{d}V - \int_{V_0} \delta\mathbf{u}\cdot\mathbf{b}_0\,\mathrm{d}V - \int_{\Gamma_0} \delta\mathbf{u}\cdot\mathbf{t}_0\,\mathrm{d}\Gamma \tag{5}$$

where $\mathbf{S}$ is the second Piola–Kirchhoff stress tensor and is related to the Cauchy stress tensor via the standard relation $\boldsymbol{\sigma} = \mathbf{F}\mathbf{S}\mathbf{F}^{\mathrm{T}}/J$; $\mathbf{E}$ is the Green–Lagrange strain tensor and is defined by $E_{ij} = (u_{i,j} + u_{j,i} + u_{k,i}u_{k,j})/2$; and $\mathbf{b}_0$ and $\mathbf{t}_0$ are the body force vector and the traction vector in the reference configuration, respectively. Eq. (5) can be linearized and cast in the Newton–Raphson framework as

$$\delta W(\delta\mathbf{u}, V_0) + D_{\mathrm{int}}\delta W(\delta\mathbf{u}, V_0)\Delta\mathbf{u} = 0 \tag{6}$$

Since Eq. (5) is linear with respect to the external work expressions, the linearization of the external virtual work vanishes. Eq. (5), however, is nonlinear with respect to the internal energy and its linearization leads to the following form:

$$D_{\text{int}}\delta W(\delta\mathbf{u}, V_0)\Delta\mathbf{u} = \int_{V_0} \left(\delta\mathbf{E} : D\mathbf{S} + \mathbf{S} : D(\delta\mathbf{E})\right) \mathrm{d}V$$
$$= \int_{V_0} \delta\mathbf{E} : \mathbf{C} : D\mathbf{E}\, \mathrm{d}V + \int_{V_0} \mathbf{S} : D(\delta\mathbf{E})\, \mathrm{d}V \tag{7}$$

Re-writing Eq. (7) in the rate form and using standard relation to rearrange Eq. (7) in the current configuration, the updated Lagrangian formulation reads

$$\int_{V_{n+1}} \nabla(\delta\mathbf{u}) : \Delta\boldsymbol{\sigma}\, \mathrm{d}V + \int_{V_{n+1}} \nabla(\delta\mathbf{u}) : (\boldsymbol{\sigma}_n \otimes \mathbf{1}) : \nabla(\Delta\mathbf{u})\, \mathrm{d}V$$
$$= \int_{V_{n+1}} \delta\mathbf{u}\cdot\mathbf{b}\, \mathrm{d}V + \int_{\Gamma_{n+1}} \delta\mathbf{u}\cdot\mathbf{t}\, \mathrm{d}\Gamma - \int_{V_{n+1}} \nabla(\delta\mathbf{u}) : \boldsymbol{\sigma}_n\, \mathrm{d}V \tag{8}$$

In order to use the Cauchy stress and the linear strain in constitutive laws, a frame indifferent stress rate is used in Eq. (8). For finite deformation, the use of constitutive equations in rate form is desirable. In large-deformation analysis, equations of this type ought to be written in terms of objective rates to maintain correct rotational transformation properties. Rate constitutive relations can be alternatively formulated in a material or a spatial setting. The former case involves rates of material tensors that are always objective. In a spatial formulation, however, material rates of objective tensors are not objective and are commonly referred to as objective stress rates such as the Jaumann rate. In a spatial setting, these equations express a relationship between some objective rate of a spatial stress tensor such as the Cauchy or Kirchhoff stress tensor, and the rate of deformation. In contrast to small deformation, the strain rate for the small deformation will be replaced by the rate of deformation. The Jaumann stress rate of the Cauchy stress tensor is used [11–13] and reads

$$\frac{\mathrm{D}\boldsymbol{\sigma}}{\mathrm{D}t} = \dot{\boldsymbol{\sigma}}^{\mathrm{J}} + \boldsymbol{\omega}\cdot\boldsymbol{\sigma} + \boldsymbol{\sigma}\cdot\boldsymbol{\omega}^{\mathrm{T}} = \mathbf{C}^{\mathrm{J}}_{\mathrm{EI}} : \mathbf{D} + \boldsymbol{\omega}\cdot\boldsymbol{\sigma} + \boldsymbol{\sigma}\cdot\boldsymbol{\omega}^{\mathrm{T}} \tag{9}$$

The rate of the Cauchy stress tensor $\dot{\boldsymbol{\sigma}}$ is written in terms of the spin invariant Jaumann stress rate. The superscript 'J' denotes Jaumann's stress rate. The material derivative of the Cauchy stress consists of two parts: the rate of change due to material response, which is reflected in the objective rate, and the change of stress due to finite rotation, which corresponds to the last two terms. $\mathbf{D}$ is the rate of deformation and the symmetric part of the velocity gradient $\mathbf{L}$, which is given by

$$\mathbf{D} = \frac{1}{2}\left(\nabla\mathbf{v} + \nabla^{\mathrm{T}}\mathbf{v}\right) = \frac{1}{2}\left(\mathbf{L} + \mathbf{L}^{\mathrm{T}}\right) = \dot{\boldsymbol{\varepsilon}} \tag{10}$$

$$\boldsymbol{\omega} = \frac{1}{2}\left(\nabla\mathbf{v} - \nabla^{\mathrm{T}}\mathbf{v}\right) = \frac{1}{2}\left(\mathbf{L} - \mathbf{L}^{\mathrm{T}}\right) \tag{11}$$

The effective spin with respect to the current configuration, $\boldsymbol{\Omega}$, can be given as

$$\boldsymbol{\Omega} = \boldsymbol{\omega}\Delta t = \frac{1}{2}\left(\nabla\Delta\mathbf{u} - \nabla^{\mathrm{T}}\Delta\mathbf{u}\right) \tag{12}$$

The incremental strain with respect to the current configuration is given by

$$\Delta\boldsymbol{\varepsilon} = \mathbf{D}\Delta t \tag{13}$$

Therefore the incremental stress tensor takes the form

$$\Delta\boldsymbol{\sigma} = \dot{\boldsymbol{\sigma}}\,\Delta t = \mathbf{C}^{\mathrm{J}}_{\mathrm{EI}} : \Delta\boldsymbol{\varepsilon} + \left(\boldsymbol{\Omega}\cdot\boldsymbol{\sigma}_n + \boldsymbol{\sigma}_n\cdot\boldsymbol{\Omega}^{\mathrm{T}}\right) \tag{14}$$

As emphasized by Taylor and Becker [14], Eq. (14) has the appearance of a forward difference integration because the stress tensor is used at the beginning of the current time step. This treatment can simplify the calculation of stiffness matrix derived from Eq. (8). Inserting Eq. (14) into Eq. (8), the updated Lagrangian formulation is obtained based on the Jaumann stress rate and reads

$$\int_{V_{n+1}} \nabla(\delta\mathbf{u}) : \mathbf{C} : \Delta\boldsymbol{\varepsilon}\, \mathrm{d}V + \int_{V_{n+1}} \nabla(\delta\mathbf{u}) : \left(\boldsymbol{\Omega}\boldsymbol{\sigma}_n + \boldsymbol{\sigma}_n\boldsymbol{\Omega}^{\mathrm{T}}\right) \mathrm{d}V + \int_{V_{n+1}} \nabla(\delta\mathbf{u}) : (\boldsymbol{\sigma}_n \otimes \mathbf{1}) : \nabla(\Delta\mathbf{u})\, \mathrm{d}V$$
$$= \int_{V_{n+1}} \delta\mathbf{u}\cdot\mathbf{b}\, \mathrm{d}V + \int_{\Gamma_{n+1}} \delta\mathbf{u}\cdot\mathbf{t}\, \mathrm{d}\Omega - \int_{V_{n+1}} \nabla(\delta\mathbf{u}) : \boldsymbol{\sigma}_n\, \mathrm{d}V \tag{15}$$

The use of the Jaumann stress rate simplifies the stress integration algorithm, which enables the use of similar solution strategy of small deformation for large deformation. Based on Eq. (15), one can see that the tangent stiffness for large deformation includes two parts: the standard material stiffness and initial stress stiffness. With the introduction of the finite element interpolation and the discretization of the linearized weak form of Eq. (15), the incremental displacement $\Delta\mathbf{u}$ at any point within the element can be expressed in terms of nodal degree of freedom as

$$\Delta\mathbf{u}^h = \mathbf{N}\Delta\mathbf{u}^e \tag{16}$$

$$\Delta\boldsymbol{\varepsilon}^h = \mathbf{B}\Delta\mathbf{u}^e, \qquad \Delta\boldsymbol{\Omega}^h = \mathbf{B}^w\Delta\mathbf{u}^e \tag{17}$$

The test function is given by

$$\left(\delta\mathbf{u}^h\right)^{\mathrm{T}} = \left(\delta\mathbf{u}^e\right)^{\mathrm{T}}(\mathbf{N})^{\mathrm{T}} \tag{18}$$

Inserting Eqs. (16) to (18) into Eq. (15), one can obtain the matrix form of the updated Lagrangian formulation:

$$\mathop{\mathbf{A}}_{e=1}^{NEL}\left(\delta\mathbf{u}^e\right)^{\mathrm{T}}\cdot\left(\mathbf{K}_{\mathrm{M}}^e+\mathbf{K}_{\mathrm{G}}^e+\mathbf{K}_{\Omega}^e\right)\cdot\Delta\mathbf{u}^e=\mathop{\mathbf{A}}_{e=1}^{NEL}\mathbf{R}^e \tag{19}$$

where

$$\mathbf{K}_{\mathrm{M}}^e=\int_{V_{n+1}^e}\mathbf{B}^{\mathrm{T}}\mathbf{C}\mathbf{B}\,\mathrm{d}V \quad \text{(material stiffness)} \tag{20}$$

$$\mathbf{K}_{\mathrm{G}}^e=\int_{V_{n+1}^e}\mathbf{G}^{\mathrm{T}}(\boldsymbol{\sigma}\otimes\mathbf{1})\mathbf{G}\,\mathrm{d}V \quad \text{(geometric nonlinear part)} \tag{21}$$

$$\mathbf{K}_{\Omega}^e=\int_{V_{n+1}^e}\left(\mathbf{B}^w\right)^{\mathrm{T}}\boldsymbol{\sigma}\boldsymbol{\Omega}^{\mathrm{T}}\,\mathrm{d}V+\int_{V_{n+1}^e}\left(\mathbf{B}^w\right)^{\mathrm{T}}\boldsymbol{\Omega}\boldsymbol{\sigma}\,\mathrm{d}V \quad \text{(finite rotation part)} \tag{22}$$

$$\mathbf{R}^e=\int_{V_{n+1}^e}\mathbf{N}\cdot\mathbf{b}\,\mathrm{d}V+\int_{\Gamma_{n+1}^e}\mathbf{N}\cdot\mathbf{t}\,\mathrm{d}\Gamma-\int_{V_{n+1}^e}\mathbf{B}\boldsymbol{\sigma}_n\,\mathrm{d}V \tag{23}$$

$$\mathbf{G}=\left[\begin{array}{cccccc}\nabla N_1 & \cdots & \nabla N_i & \cdots & \nabla N_{nen}\end{array}\right] \tag{24}$$

where the operator of ∇N_i for a three dimensional problem is given by

$$\nabla^{\mathrm{T}}N_i=\left[\begin{array}{ccccccccc}\frac{\partial N_i}{\partial x_1} & \frac{\partial N_i}{\partial x_2} & \frac{\partial N_i}{\partial x_3} & 0 & 0 & 0 & 0 & 0 & 0\\ 0 & 0 & 0 & \frac{\partial N_i}{\partial x_1} & \frac{\partial N_i}{\partial x_2} & \frac{\partial N_i}{\partial x_3} & 0 & 0 & 0\\ 0 & 0 & 0 & 0 & 0 & 0 & \frac{\partial N_i}{\partial x_1} & \frac{\partial N_i}{\partial x_2} & \frac{\partial N_i}{\partial x_3}\end{array}\right] \tag{25}$$

Eqs. (20) to (22) are the standard material, geometric element stiffness matrices and residual vector, respectively. The global stiffness matrix can be obtained by assembling the finite element stiffness and residual vector together and can be given as

$$\left[\mathop{\mathbf{A}}_{e=1}^{NEL}\left(\mathbf{K}_{\mathrm{M}}^e+\mathbf{K}_{\mathrm{G}}^e+\mathbf{K}_{\Omega}^e\right)\right]\Delta\mathbf{u}=\mathbf{F}_{\mathrm{nodal}}+\mathop{\mathbf{A}}_{e=1}^{NEL}\left(\mathbf{R}^e\right) \tag{26}$$

4. Constitutive equations and their numerical integration

4.1. Smooth three-surface Cap model

Soil compaction cannot be modeled with J_2 elastoplastic model, which does not involve volumetric plastic deformation. The Cap model is a good choice for soil compaction prediction. Fig. 1 shows a smooth surface Cap model proposed by [15].

The three-surface smooth Cap model is composed of three yield functions, $f_m(\boldsymbol{\sigma},k)$ $(m=1,2,3)$, which are expressed as follows:

$$f_1(\boldsymbol{\sigma})=\|\mathbf{s}\|-F_{\mathrm{e}}(I_1)\leqslant 0 \quad \text{(compression Cap part)} \tag{27}$$

$$f_2(\boldsymbol{\sigma},k)=\|\mathbf{s}\|^2-F_{\mathrm{c}}(I_1,k)\leqslant 0 \quad \text{(Drucker–Prager part)} \tag{28}$$

$$f_3(\boldsymbol{\sigma})=\|\mathbf{s}\|^2-F_{\mathrm{t}}(I_1)\leqslant 0 \quad \text{(tension part)} \tag{29}$$

where $\mathbf{s}$ is the deviatoric stress tensor. The specific forms of F_{e}, F_{c}, and F_{t} are defined as:

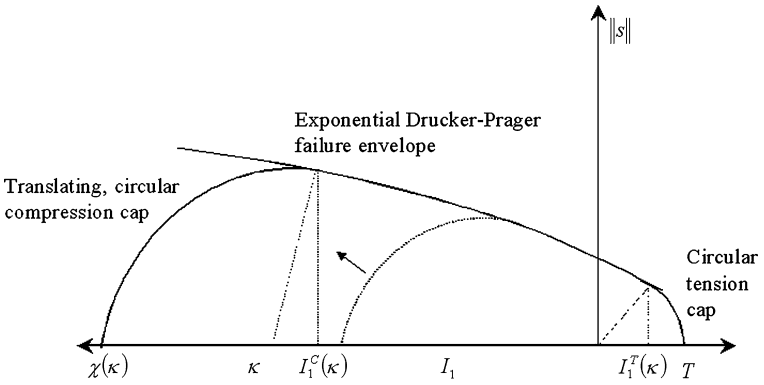

Fig. 1. Smooth three-surface two invariant Cap model.

$$F_e(I_1) = \alpha + \lambda\left[1 - \exp(\beta I_1)\right] \quad I_1^C(k) \leqslant I_1 \leqslant I_1^T \tag{30}$$

$$F_c(I_1, k) = R^2(k) - (I_1 - k)^2 \quad I_1 < I_1^C(k) \tag{31}$$

$$F_t(I_1) = R_T^2 - I_1^2 \quad I_1 > I_1^T \tag{32}$$

where F_e, F_c, and F_t are called the Drucker–Prager envelope function, the compression cap function, and the tension cap function, respectively. $\chi(k) = k - RF_e(k)$ is the point of intersection of the cap with the I_1 axis. There is a smooth transition from one surface to the next. Parameters α, λ and β are the material constants, and I_1^T is the trace of the tensile stress which denotes the critical point between the tension cap and the Drucker–Prager envelope. $I_1^C(k)$ is the trace of the compressive stress and represents the intermediate point between the Drucker–Prager envelope and the compression cap, and R_T denotes the fixed radius of the tension cap. The hardening law for this model is derived from the assumption that the plastic volumetric strain is of an exponential form given by

$$\varepsilon_v^p = -W\left\{1 - \exp\left[D\chi(k)\right]\right\} \tag{33}$$

where ε_v^p is the effective plastic volumetric strain in the soil as measured from a completely loading process. W represents the maximum possible plastic volumetric strain for the medium, with the reference state being the materials unloaded state, and D is a model parameter.

4.2. Numerical integration of the constitutive equation

The stress components are referred to a fixed coordinate system instead of corotational coordinate system, and the stress from time t_n to time t_{n+1} must also be rotated to account for the rigid body rotation that occurs in the increment [11]. In this model, the Cauchy stress is used and expressed in terms of the Jaumann rate, which is denoted by the superscript J. The rate of deformation tensor, **D**, can be decomposed into elastic and inelastic parts:

$$\mathbf{D} = \mathbf{D}^e + \mathbf{D}^p \tag{34}$$

The elastic response can be represented by the hypoelastic law, given as:

$$\Delta\boldsymbol{\sigma}^J = \mathbf{C}_E^J : \mathbf{D}^e \Delta t = \mathbf{C}_E^J : \left(\mathbf{D} - \mathbf{D}^p\right)\Delta t = \mathbf{C}_E^J : \left(\Delta\boldsymbol{\varepsilon} - \Delta\boldsymbol{\varepsilon}^p\right) \tag{35}$$

The objectivity requires that elastic modulus $\mathbf{C}_E^J$ should be isotropic. Otherwise, it will change as the material rotates due to its expression in terms of a fixed coordinate system by the push-forward.

As the rate of deformation is used to calculate the incremental strain with respect to the current configuration for large deformation, the return mapping algorithm for the finite inelasticity is the same as the small strain formulation. From the converged solution at time $t = t_n$, one can obtain the solution at time $t = t_{n+1}$ by integrating the rate constitutive equations. The operator-splitting, elastic-predictor and inelastic-corrector method was used to integrate the constitutive equation [12,13]. The two-step algorithm for stress update is summarized as follows.

Elastic predictor: It is assumed that in the interval $[t_n, t_{n+1}]$ no inelastic deformation occurs, thus the trial value is:

$$\lambda^{tr} = 0 \tag{36}$$

$$\boldsymbol{\sigma}_{n+1}^{tr} = \boldsymbol{\sigma}_n + \Delta\boldsymbol{\sigma} = \boldsymbol{\sigma}_n + \boldsymbol{\Omega}_n \cdot \boldsymbol{\sigma}_n + \boldsymbol{\sigma}_n \cdot \boldsymbol{\Omega}_n^T + \mathbf{C}_E^J : \mathbf{D}\Delta t \tag{37}$$

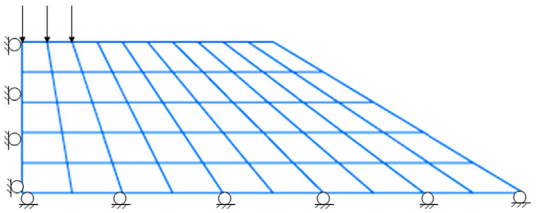

Fig. 2. (Color online.) Schematic diagram of the smooth strip footing for soil compaction.

One can obtain the equivalent relationship as follows:

$$\boldsymbol{\sigma}_n + \boldsymbol{\Omega}_n \cdot \boldsymbol{\sigma}_n + \boldsymbol{\sigma}_n \cdot \boldsymbol{\Omega}_n^{\mathrm{T}} = \mathbf{R}_n \cdot \boldsymbol{\sigma}_n \cdot \mathbf{R}_n^{\mathrm{T}} \tag{38}$$

where **R** is rotation matrix. If the elastic trial state is admissible, it indicates that inelastic deformation does not occur. Thus, the second part of the algorithm is not needed. If the elastic trial state is not admissible, a correction will be needed to determine the plastic solution state.

Plastic corrector: The inelastic strain and stress can be written as:

$$\Delta\boldsymbol{\varepsilon}^{\mathrm{p}} = \mathbf{D}^{\mathrm{p}}\Delta t = \lambda\frac{\partial f(\boldsymbol{\sigma})}{\partial\boldsymbol{\sigma}} \tag{39}$$

where λ is the plastic consistency parameter and is computed via local Newton iteration of the discrete constitutive equation emanating from the smooth surface constitutive equation. When taking non-zero values, the incremental inelastic strain and Cauchy stress tensor can be written as

$$\boldsymbol{\sigma}_{n+1} = \boldsymbol{\sigma}_n + \Delta\boldsymbol{\sigma} = \boldsymbol{\sigma}_n + \boldsymbol{\Omega}\boldsymbol{\sigma}_n + \boldsymbol{\sigma}_n\boldsymbol{\Omega} + \mathbf{C}_{\mathrm{E}}^{\mathrm{J}} : \left(\Delta\boldsymbol{\varepsilon} - \Delta\boldsymbol{\varepsilon}^{\mathrm{p}}\right) \tag{40}$$

The tangent modulus for the three parts of the Cap model can be obtained by taking the derivative of incremental stress tensor due to Jaumann rate,

$$\mathbf{C}_{\mathrm{EI}}^{\mathrm{J}} = \frac{\partial\Delta\boldsymbol{\sigma}}{\partial\Delta\boldsymbol{\varepsilon}} \tag{41}$$

The fourth-order continuum tangent modulus tensor can be used in a similar way to the conventional elastoplastic tangent modulus. The above formulations were implemented in FEAP [16].

5. Numerical examples

In this section, three numerical examples are provided to show the effectiveness of large-deformation finite-element formulation for soil compaction prediction in geotechnical and pavement engineering.

5.1. Static soil compaction

The aim of this numerical example is to demonstrate the large deformation finite-element formulation for static soil compaction. The numerical test simulates the soil compaction of an embankment strip footing. The horizontal extent of the stratum is 6.096 m from the footing center, and the depth of the stratum is 0.914 m. The slope of the embankment is 0.6 on both sides. Due to the symmetrical nature of the problem, only half of the physical domain is discretized for analysis. The boundary conditions are fixed in the direction of thickness as shown in Fig. 2, and they result in plane strain conditions. The initial density is 2000 kg/m^3 (to be consistent with the next simulation) ton/m^3. Young's modulus E and Poisson's ratio ν are 239.0 MPa and 0.3, respectively. The constitutive parameters for the smooth surface Cap model are: $\alpha = 0.143$ MPa, $\lambda = 0.217$ MPa, $\beta = 1.32 \times 10^{-6}$ Pa^{-1}, $W = 0.003$, $D = 1.59 \times 10^{-6}$ Pa^{-1}, and $\kappa_0 = -1.67$ MPa. For the large-deformation formulation, the contours of the spatial density are projected onto the initial and intermediate deformed configurations in Figs. 3–5, which clearly show the increase of spatial density underneath the loading area. The density variation is a technical index of soil stabilization, and therefore it is a quantity of practical importance in geotechnical engineering. After compaction, these figures indicate that the spatial density is redistributed and the maximum density increases from 2.0 ton/m^3 to 3.14 ton/m^3. These figures clearly demonstrate that the proposed large deformation finite-element formulation can be used to predict the soil compaction process in geotechnical engineering.

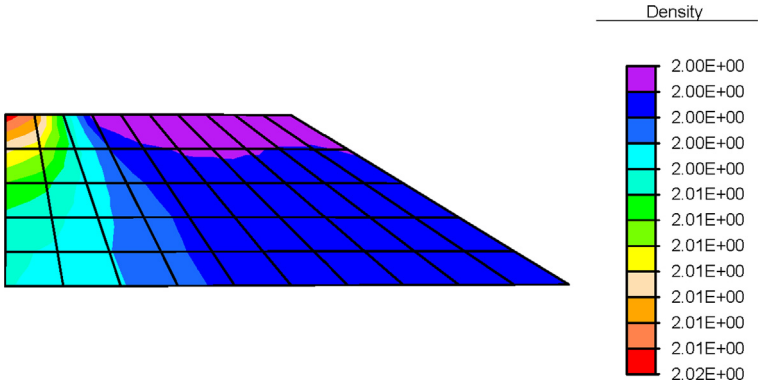

Fig. 3. (Color online.) Spatial density contour projected onto deformed configuration at pseudo time $t = 0.0$.

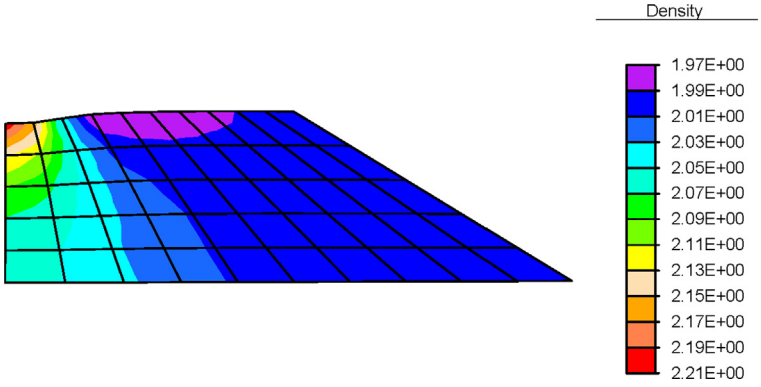

Fig. 4. (Color online.) Spatial density contour projected onto deformed configuration at pseudo time $t = 0.6$.

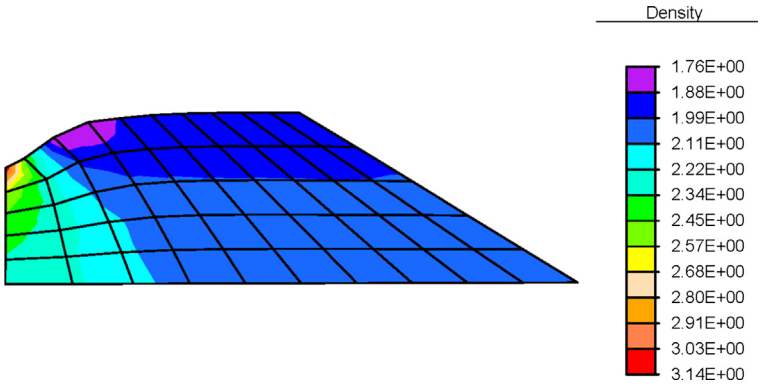

Fig. 5. (Color online.) Spatial density contour projected onto deformed configuration at pseudo time $t = 1.0$.

5.2. Plane strain footing foundation problem

This numerical test simulates the elastoplastic soil compaction in a strip footing problem. The physical domain is a 1.57-m-wide strip footing, resting on a shallow stratum supported by a rigid and perfectly rough base. The horizontal extent of the stratum is 7.32 m from the footing center, and the depth of the stratum is 3.66 m. The boundary conditions are fixed in the direction of thickness as shown in Fig. 6. Because of symmetry, only half of the physical domain is discretized. A uniform mesh of $14 \times 7 \times 1$ hexahedral elements is employed, which is the same as that used in literature [17]. The initial density is 2000 kg/m^3. The Young modulus E and the Poisson ratio ν are 206.7 MPa and 0.3, respectively. The constitutive parameters for the smooth surface Cap model are: $\alpha = 0.129$ MPa, $\lambda = 0.120$ MPa, $\beta = 1.32 \times 10^{-6}$ Pa^{-1}, $W = 0.003$, $D = 1.59 \times 10^{-6}$ Pa^{-1}, and $\kappa_0 = -1.67$ MPa. The complete load–displacement response for the strip footing is shown in Fig. 7, where the applied base pressure is plotted versus the centerline subsidence directly beneath the footing for each case [17]. Both small deformation and large-deformation results were simulated (see Fig. 7). For the same base pressure, the

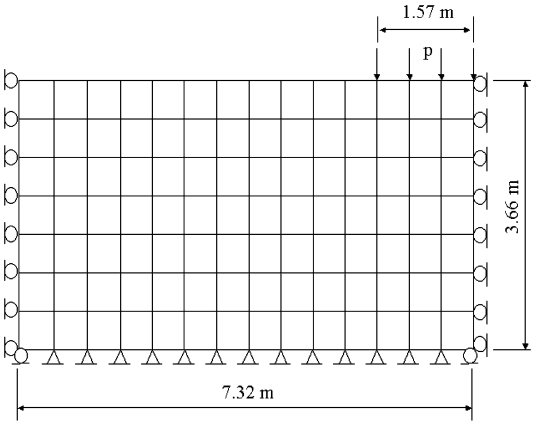

Fig. 6. Schematic diagram of the smooth strip footing for soil compaction.

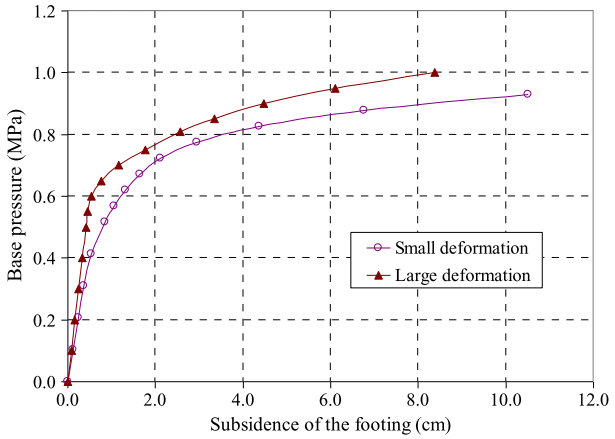

Fig. 7. External load versus subsidence induced by flexible footing loading.

subsidence obtained by small deformation is relatively larger than that of large deformation. The reason is that the stiffness of large deformation has an additional stiffness term, which results from the initial stress stiffness. Fig. 8 shows the vertical stress at an integral point of the top left element versus the footing pressure. The stress state in the element is in nearly hydrostatic compression state. The stress-footing pressure curve indicates that the material point initially deforms elastically and thereafter enters the plastic range. After further compaction, the soil becomes stiffer due to volumetric hardening. Trends similar to that in the simulation using the Cap model were also obtained by [18,19]. Figs. 9 and 10 show the pressure contours projected onto the initial and intermediate deformed configuration. The deformation is magnified at the scale of 10 in the contour plots. A smooth hydrostatic stress profile is obtained in the entire range of deformation. Based on the mass conservation and on the obtained subsequent configurations, the contour of the spatial density projected onto the initial and intermediate deformed configurations are presented in Figs. 11 and 12. A literature review reveals that very few research efforts have been paid using the finite-element method to predict compaction density induced by external loads. The proposed large-deformation finite-element formulation is a new attempt as regards this aspect.

5.3. Prediction of the compacted density

This numerical test is used to further demonstrate the application of large-deformation model to predict spatial density changes induced during compaction of the soil. A quarter of the physical domain (4 m in length, 4 m in width and 2 m in depth) is compacted by a uniformly distributed load of 40 kN/m^2 applied on the top surface. (See Fig. 13.) Symmetry boundary conditions are applied along the planes passing through $(x, y, z) = (0, 0, 0)$. An unstructured mesh of $4 \times 4 \times 7$ hexahedral elements is employed. The original density is 2 ton/m^3. Young's modulus E and Poisson's ratio ν are 5.0 MPa and 0.3, respectively. The constitutive parameters for the smooth surface Cap model are: $\alpha = 0.129$ MPa, $\lambda = 0.120$ MPa, $\beta = 1.32 \times 10^{-6}$ Pa^{-1}, $W = 0.003$, $D = 1.59 \times 10^{-6}$ Pa^{-1}, and $\kappa_0 = -1.67$ MPa.

In order to examine the stability performance of the large-deformation formulation, both coarse and fine meshes are used in this example study. Fig. 14 shows the change in density at the top corner point, where the maximum compaction density is attained for this simulation. The density converges to a value that is dependent on the Cap model parameters as well

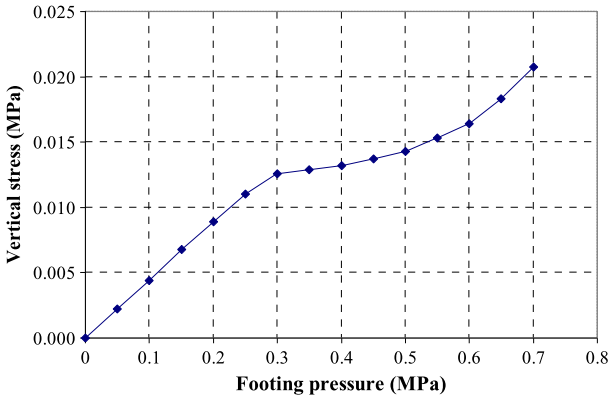

Fig. 8. Vertical stress versus the footing pressure.

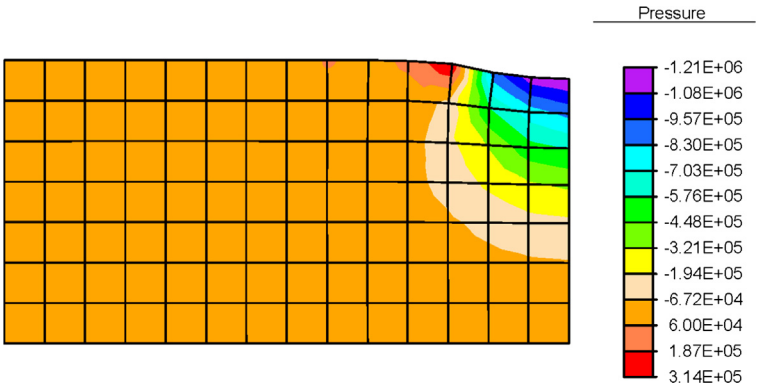

Fig. 9. (Color online.) Pressure contours projected onto an intermediate deformed configuration (base pressure is 0.5 MPa).

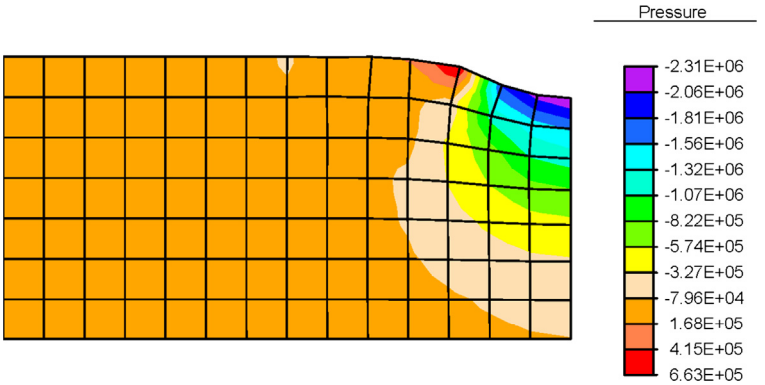

Fig. 10. (Color online.) Pressure contours projected onto an intermediate deformed configuration (base pressure is 0.6 MPa).

as on the applied loads. Since the compaction density is calculated at the integration points, for plotting purpose, they are projected onto the nodal points. Fig. 14 shows the compaction densities from both fine and coarse meshes to demonstrate the stability performance of the large-deformation formulation. Figs. 15 and 16 show the vertical stress contours projected on two deformed configurations at two different load levels. A smooth stress profile is attained in the entire range of deformation. The contours of the spatial density projected onto two intermediate deformed configurations are presented in Figs. 17 and 18 for three different load levels. The maximum density is located at the top corner point, which increases with increasing load level.

6. Concluding remarks

A three-dimensional large-deformation finite-element formulation for modeling soil compaction is presented in this paper. An updated Lagrangian formulation is used that allows the use of the weak forms that, involving integrals, are taken

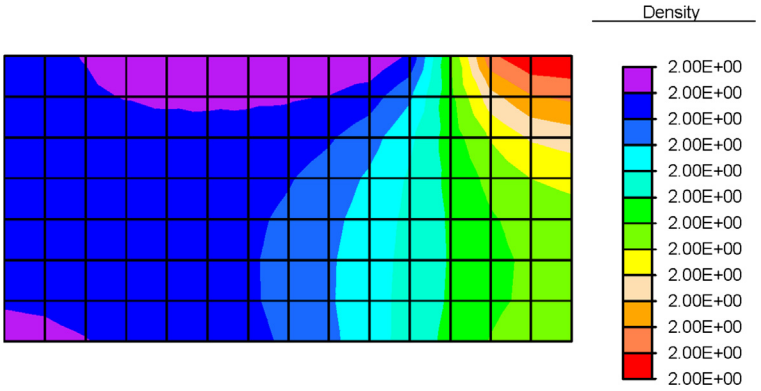

Fig. 11. (Color online.) Spatial density contours projected onto an intermediate deformed configuration (base pressure is 0.05 MPa).

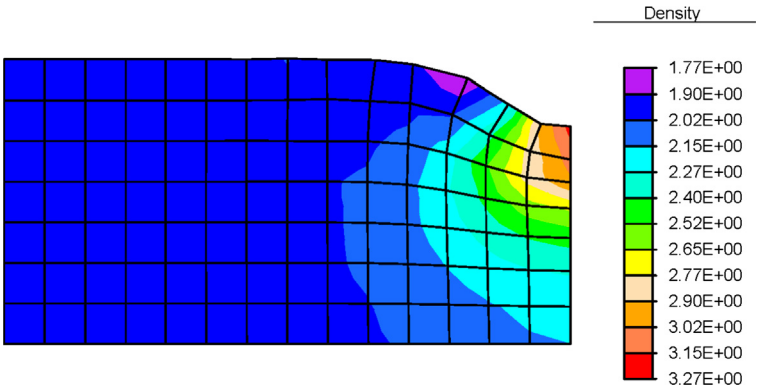

Fig. 12. (Color online.) Spatial density contours projected onto an intermediate deformed configuration (base pressure equal to 0.7 MPa).

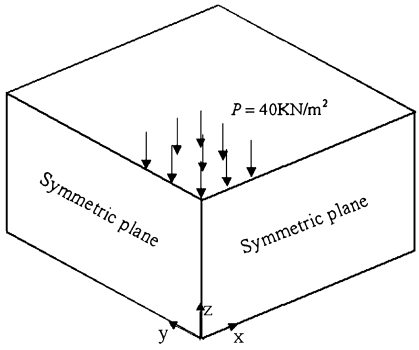

Fig. 13. Schematic diagram of the problem.

with respect to the current configuration. Therefore, it is well suited for modeling compaction in geotechnical engineering. The rate of deformation is used as the measure of strain rate for the updated Lagrangian formulation. In order to keep the principle of objectivity, an objective integration algorithm with Jaumann's stress rate is employed to account for the rotation of the stress in a superimposed rigid body motion. As a result, the objective rate of stress to maintain correct rotational transformation properties is maintained, which allows the use of Cauchy stress and the linear strain in constitutive laws. Representative simulations of soil compaction are conducted for the cases of static embankment compaction, plane strain footing. Our numerical results show that the large-deformation finite-element formulation is a good approach to predict the spatial density change due to compaction, which differentiates the general estimates in terms of settlement. This study provides an efficient approach to simulate the spatial density due to the compaction of the granular materials, which is a very critical issue in geotechnical, pavement, and agricultural engineering.

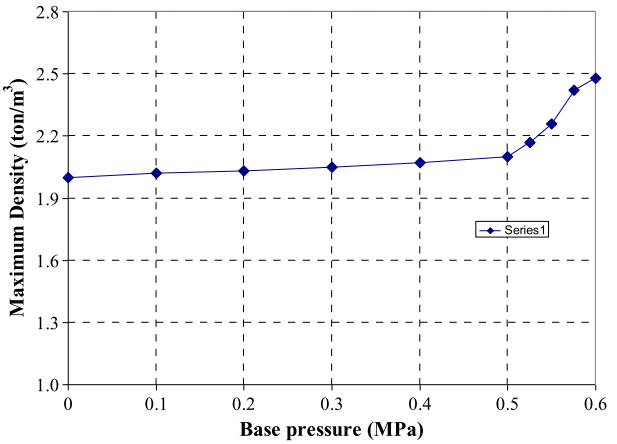

Fig. 14. Compaction density versus load for fine and coarse meshes.

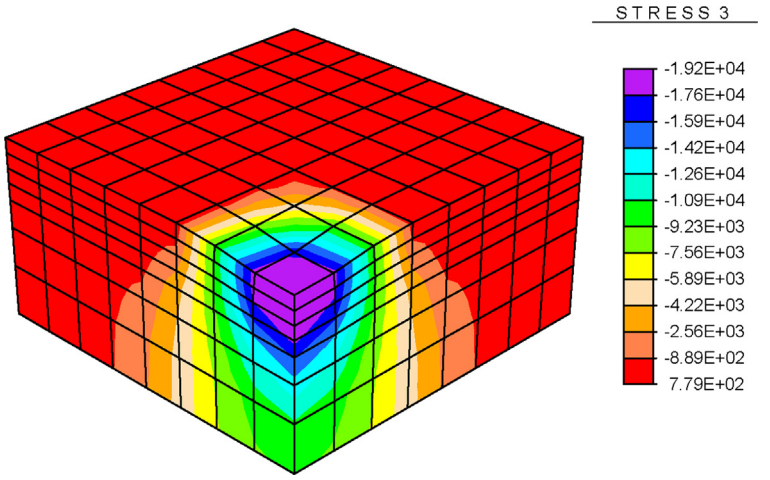

Fig. 15. (Color online.) Stress σ_{zz} contour projected on deformed coarse mesh configuration at $t_n = 0.5$.

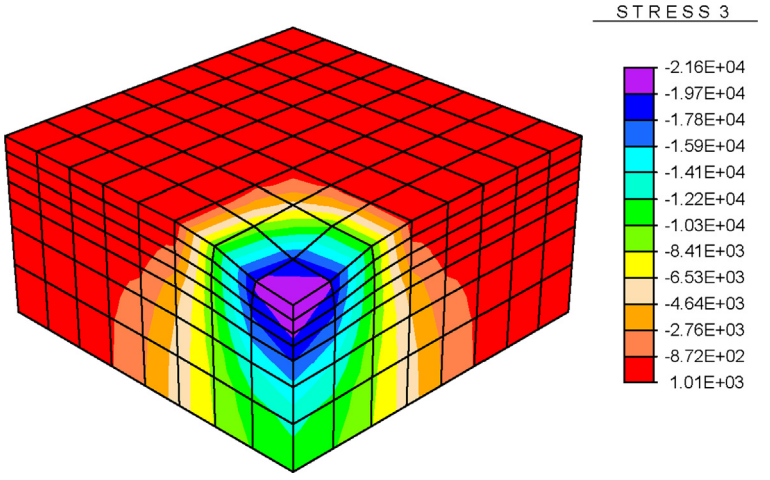

Fig. 16. (Color online.) Stress σ_{zz} contour projected on deformed coarse mesh configuration at $t = 0.55$.

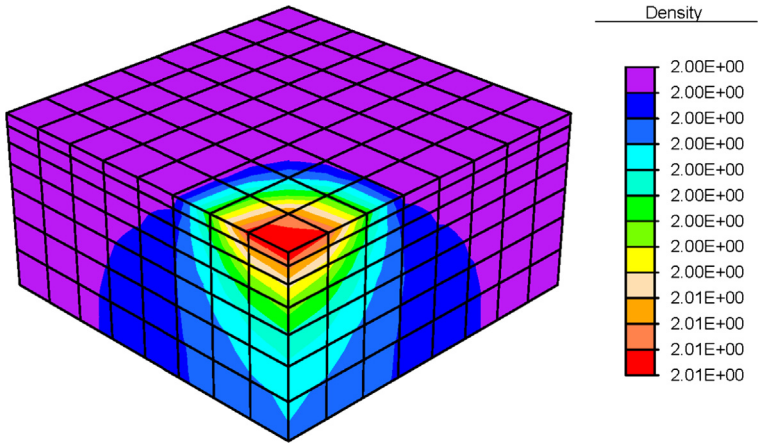

Fig. 17. (Color online.) Spatial density contour projected on deformed coarse mesh configuration at $t = 0.05$.

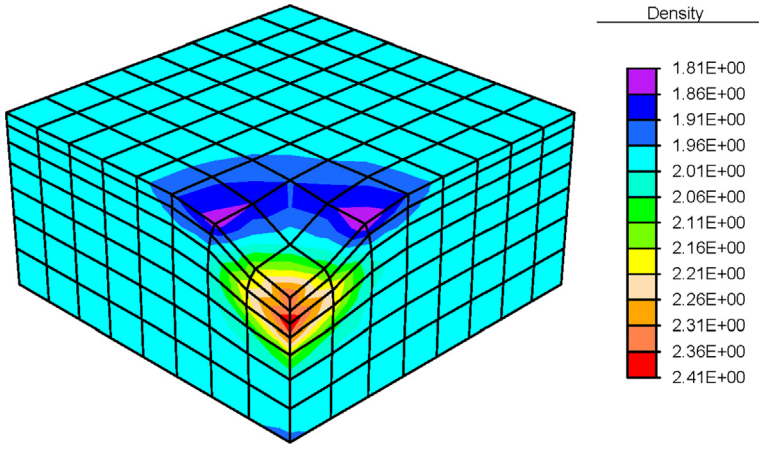

Fig. 18. (Color online.) Spatial density contour projected on deformed coarse mesh configuration at $t = 0.6$.

References

[1] T. Eguchi, T. Muro, Measurement of compacted soil density in a compaction of thick finishing layer, J. Terramech. 44 (2007) 347–353.
[2] S. Kimmel, M. Mooney, Real-time soil compaction monitoring through pad strain measurements, in: Proc. Smart Structures/Nondestructive Evaluation, San Diego, CA, USA, 2011.
[3] D. Pietzsch, W. Poppy, Simulation of soil compaction with vibratory roller, J. Terramech. 29 (1992) 585–597.
[4] D. Montgomery, Stabilized soil research progress report SSRPR06, School of Engineering, University of Warwick, UK, 1999.
[5] E. Canillas, V. Salokhe, Modeling compaction in agricultural soils, J. Terramech. 39 (2002) 71–84.
[6] F.H. Lee, T. Gu, Method for estimating dynamic compaction effect on sand, J. Geotech. Geoenviron. Eng. 130 (2004) 139–152.
[7] K. Carman, Prediction of soil compaction under pneumatic tires using fuzzy logic approach, J. Terramech. 45 (2008) 103–108.
[8] K. Xia, L. Chi, A viscoplastic foam model for prediction of asphalt pavement compaction, in: ASCE Geotechnical Special Publication Series, vol. 182, 2008, pp. 136–145.
[9] H. Brandl, F. Kopf, D. Adam, Continuous compaction control (CCC) with different dynamic rollers, Heft 553, ISSN 0379-1491, Wien, Austria, 2005.
[10] K. Mahutka, J. Grabe, Numerical investigation of soil compaction and vibration propagation due to strong dynamic excitation, in: Proceedings of Joint ASME/ASCE/SES Conference on Mechanics and Materials, Baton Rouge, LA, USA, 2005.
[11] T.J.R. Hughes, J. Winget, Finite rotation effects in numerical integration of rate constitutive equations arising in large-deformation analysis, Int. J. Numer. Methods Eng. 33 (1980) 1413–1449.
[12] J.C. Simo, T.J.R. Hughes, Computational Inelasticity, Springer-Verlag, 1993.
[13] T. Belytschko, W.K. Liu, B. Moran, Nonlinear Finite Elements for Continua and Structure, John Wiley & Sons Ltd., 2000.
[14] L.M. Taylor, E.B. Becker, Some computational aspects of large deformation, rate-dependent plasticity problems, Comput. Methods Appl. Mech. Eng. 41 (1983) 251–277.
[15] C.C. Swan, Y.K. Seo, A Smooth Three-Surface Elasto-Plastic Cap Model: Rate Formulation, Integration Algorithm and Tangent Operators, University of Iowa, IA, USA, 2000.
[16] R.L. Taylor, FEAP – A Finite Element Analysis Program, version 7.1, Programmer Manual, 1999.
[17] W.F. Chen, X.L. Liu, Limit Analysis in Soil Mechanics, Elsevier, 1990, pp. 1–24.
[18] G. Hofstetter, J.C. Simo, R.L. Taylor, A modified Cap model: closest point solution algorithm, Comput. Struct. 46 (1993) 202–214.
[19] K. Xia, A. Masud, A new stabilized finite-element method embedded with a Cap model for the analysis of granular material, J. Eng. Mech. 132 (2006) 250–259.